CHEMISTRY OF MATERIALS

pubs.acs.org/cm

Article

Regulating Eu^{2+} Multisite Occupation through Structural Disorder toward Broadband Near-Infrared Emission

Yingze Zhu, Xuesong Wang, Jianwei Qiao, Maxim S. Molokeev, Hendrik C. Swart, Lixin Ning,* and Zhiguo Xia*

Cite This: *Chem. Mater.* 2023, 35, 1432−1439

Read Online

ACCESS | Metrics & More | Article Recommendations | Supporting Information

ABSTRACT: To promote the development of near-infrared (NIR) light sources in optoelectronic and biomedical applications, the discovery of NIR-emitting phosphor materials and their design principles are essential. Herein, we report a novel Eu^{2+}-activated broadband NIR-emitting phosphor, $BaSrGa_4O_8:Eu^{2+}$, which features multisite occupation due to Ba/Sr and oxygen site occupancy disorder. With an increase in the Ba/Sr atomic ratio from 1:1 to 1.7:0.3, the Eu^{2+} emission band maximum red-shifts from 670 to 775 nm, along with an enlargement of the full width at half-maximum (FWHM) from 140 to 230 nm. The underlying mechanism for the structure−property relationship is elucidated using density functional theory calculations. The application of the NIR phosphor-converted light-emitting diodes (pc-LEDs) is demonstrated, showing their potential in night-vision technology. Our results can initiate further exploitation of the host structural disorder toward Eu^{2+} broadband NIR luminescence for applications in pc-LEDs.

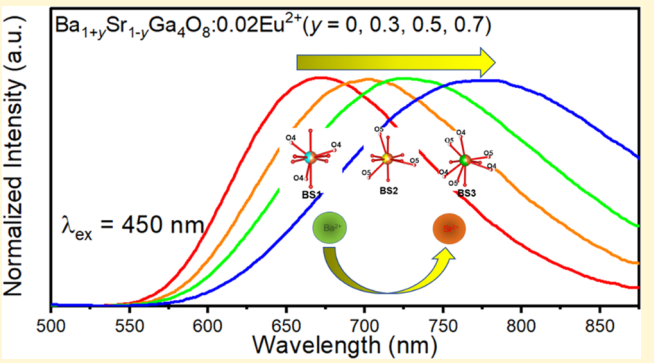

INTRODUCTION

Near-infrared (NIR) light sources play an important role in NIR spectroscopy technologies, which are widely applied in night-vision, food analysis, biomedical imaging, etc.[1−4] Traditional NIR light sources, such as tungsten−halogen lamps or NIR light-emitting diodes (LEDs), suffer from massive sizes or narrow emission spectra (full width at half maxima (FWHM) <50 nm), which are unsuitable for portable applications including daily food and health monitoring and rapid analysis where the compact size and sufficiently broad NIR emission are desired.[5] Recently, NIR-emitting phosphor-converted LEDs (pc-LEDs) have attracted considerable research interest because of their small size, tunable broadband emission, and high efficiency. However, the development of efficient and broadband NIR-emitting phosphors, especially those that can be excited by commercial ultraviolet (*n*-UV) or blue LED chips, remains a significant challenge.[6,7]

Octahedrally coordinated Cr^{3+} has been considered as an ideal luminescence center to realize broadband NIR emission in the range of 650−1200 nm due to the $^4T_2 \rightarrow {}^4A_2$ transition within the $3d^3$ configuration that can be excited by the commercial blue LED chips.[8] However, Cr^{3+} tends to be oxidized into Cr^{4+} and Cr^{6+} during high-temperature synthesis, which is toxic and also deteriorates the performance of the phosphors.[9,10] Other transition-metal ions such as Mn^{4+}, Ni^{2+}, and Fe^{3+} have also been investigated to design broadband NIR-emitting phosphors, but they generally cannot be effectively excited by blue light.[11−13] Eu^{2+}-activated phosphors normally exhibit tunable emissions in the visible range and have been widely applied in the field of commercial white LEDs.[14−16] It is worth noting that Eu^{2+}-activated NIR-emitting oxide-based phosphors, especially those that can be pumped by the commercial blue LED chips, have been reported just recently based on the pioneering work of our group.[17] Moreover, Eu^{2+}-doped nitride near-infrared phosphors that can be excited by blue light have also been reported.[18] Generally, by designing Eu^{2+} substitutions at host sites with small coordination numbers (e.g., six-coordinated sites), blue-light pumped broad NIR emissions have been achieved in a number of Eu^{2+}-activated phosphors, with the emission band maximum λ_{max} = 720−773 nm and FWHM = 120−210 nm (Table S1). It is noted that the dopants Eu^{2+} at a small host site experience relatively large crystal-field interactions with their crystalline surroundings leading to long-wavelength excitation and emission.

Generally, Eu^{2+} substitutions at multiple crystallographic sites with different coordinating environments are beneficial for

Received: December 5, 2022
Revised: January 8, 2023
Published: January 27, 2023

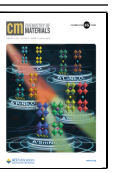

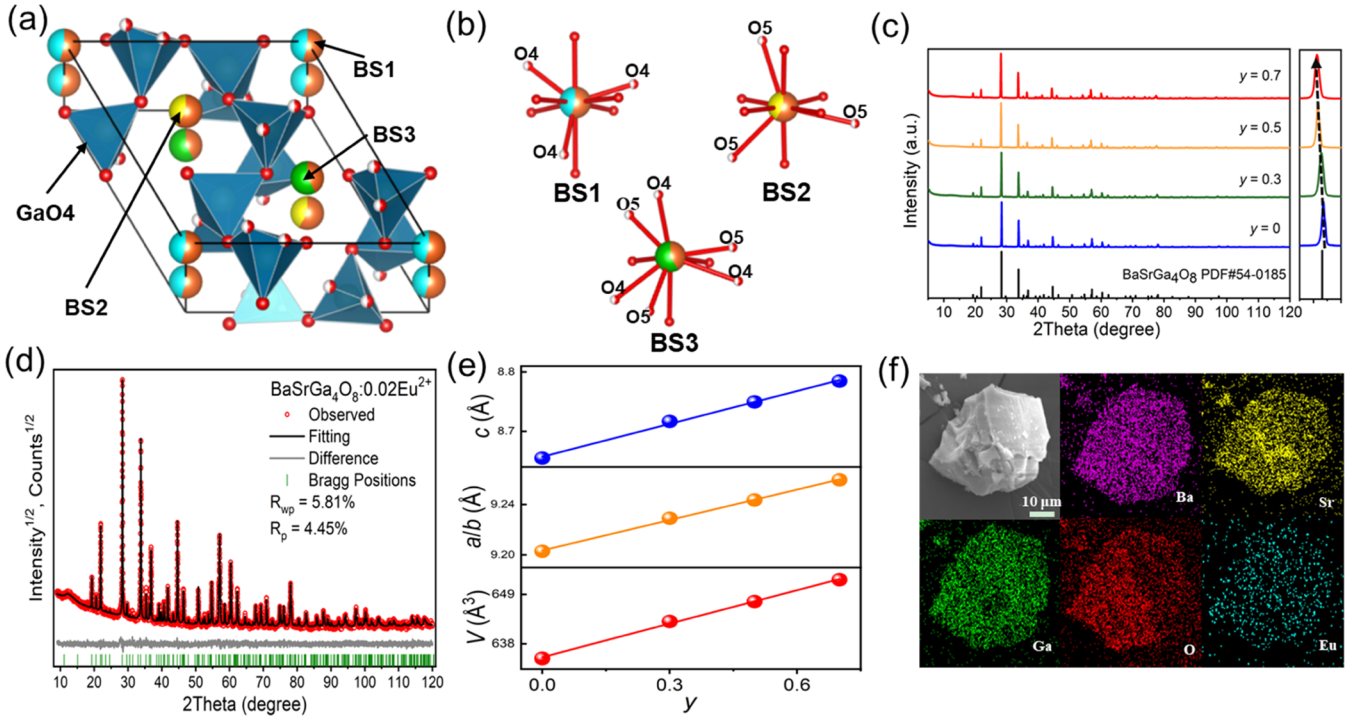

Figure 1. (a) Crystal structure diagram of $BaSrGa_4O_8$ viewed along the *c*-axis. (b) Coordination structures of BS*i* (*i* = 1−3) sites. (c) XRD pattern of $Ba_{1+y}Sr_{1-y}Ga_4O_8$:0.02Eu^{2+} (*y* = 0, 0.3, 0.5, 0.7). (d) Rietveld refinement of $BaSrGa_4O_8$:0.02Eu^{2+}. (e) Variation of lattice parameters *a*, *b*, and *c* and cell volume *V*(*y*) of $Ba_{1+y}Sr_{1-y}Ga_4O_8$:0.02Eu^{2+} (*y* = 0, 0.3, 0.5, 0.7). (f) Element-mapping images of Ba, Sr, Ga, O, and Eu for the selected $BaSrGa_4O_8$:0.02Eu^{2+} particle.

increasing the FWHM of the emission band owing to inhomogeneous band broadening. A promising strategy along this line featuring multisite substitution is to exploit the structural disorder of the host lattice, which could result in numerous distinct local coordinating environments. Accordingly, we report a novel Eu^{2+}-activated NIR-emitting phosphor $BaSrGa_4O_8$:Eu^{2+} that exhibits broadband emission at 550−900 nm under 450 nm blue-light excitation. The host material is characterized by a random occupation of Ba and Sr atoms at three crystallographic sites (referred to as BS1, BS2, and BS3 sites hereafter), together with the half occupancy at the two oxygen sites (O4 and O5 in Figure 1a). Within a cutoff bond length of 3.1 Å, the three BS sites are all nominally coordinated by nine oxygens, but actually, the BS1 and BS2 sites are each coordinated by 7.5 oxygens located at six fully- and three half-occupied O sites, and the BS3 site is surrounded by six oxygens located at three fully- and six half-occupied oxygen sites (Figure 1b). The dopants Eu^{2+} are expected to substitute at these sites owing to size and charge match. Controllable emission from λ_{max} = 670 to 775 nm was observed for $Ba_{1+y}Sr_{1-y}Ga_4O_8$:Eu^{2+} with an increase in the Ba/Sr ratio from *y* = 0 to 0.7, along with an increase of the FWHM of the emission band from 140 to 230 nm. This work represents an innovative attempt by structural design and site occupation in solid-state materials, and the targeted exploitation of structural disorder in the host material is useful for generating Eu^{2+} broadband NIR luminescence.

EXPERIMENTAL SECTION

Synthesis. $Ba_{1+y}Sr_{1-y}Ga_4O_8$:Eu^{2+} (*y* = 0, 0.3, 0.5, 0.7) powder samples were synthesized via a high-temperature solid-state reaction. According to the given stoichiometric ratios, the mixtures of high-purity $BaCO_3$ (A.R.), $SrCO_3$ (A.R.), Ga_2O_3 (99.99%), and Eu_2O_3 (99.99%) were weighed and ground in an agate mortar and transferred into an alumina crucible. They were then sintered under a reducing atmosphere (20%H_2/80%N_2) at 1300 °C for 8 h, cooled naturally to room temperature, and finely ground using a mortar for further characterization.

Characterization. The powder X-ray diffraction (PXRD) patterns of all of the samples were collected at room temperature (RT) using an Aeris PXRD diffractometer (PANalytical Corporation, Netherlands) operating at 40 kV and 15 mA with monochromatized Cu Kα radiation (λ = 1.5406 Å). Rietveld analysis of PXRD was performed using TOPAS 4.2.[19] The morphology and particle size were characterized by scanning electron microscopy (SEM) (NOVA NANOSEM 430), and the elemental mapping was performed using energy-dispersive X-ray spectroscopy (EDS) combined with SEM. The photoluminescence (PL) and photoluminescence excitation (PLE) spectra, luminescence decay curves, and temperature-dependent emission spectra were measured using an FLS1000 fluorescence spectrophotometer equipped with xenon (Xe) lamps as radiating sources. The PLQYs values were measured using an integrated sphere on the Edinburgh FLS1000 fluorescence spectrophotometer. For the NIR pc-LED lamp fabrication, a blue InGaN chip (λ_{em} = 450 nm) was combined with the selected NIR-emitting $Ba_{1.7}Sr_{0.3}Ga_4O_8$:0.02Eu^{2+} phosphor. The PL spectra of the as-fabricated NIR pc-LED were measured by Morpho 3.2 software with a NOVA Laboratory Class Spectrometer. The output spectrum and device parameters of the as-fabricated NIR pc-LED were measured using an integrating sphere spectroradiometer system (HAAS-2000, Everfine). The demonstration images were collected by a NIR and a visible camera.

Computational Methodology. Periodic density functional theory (DFT) calculations were carried out using the Perdew−Burke−Ernzerhof (PBE) functional[20] and its PBE + *U* variant with U = 2.5 eV for Eu 4f electrons,[21,22] as implemented in the VASP package.[23,24] Ba($5d^{10}6s^2$), Sr($4d^{10}5s^2$), Ga($4s^24p^1$), O($2s^22p^4$), and Eu($5s^25p^64f^76s^2$) were treated as valence electrons, and their interactions with the respective cores were described by the projected-augmented-wave approach.[25] The atomic structures were fully optimized until the total energies and the forces on the atoms

https://doi.org/10.1021/acs.chemmater.2c03631
Chem. Mater. 2023, 35, 1432−1439

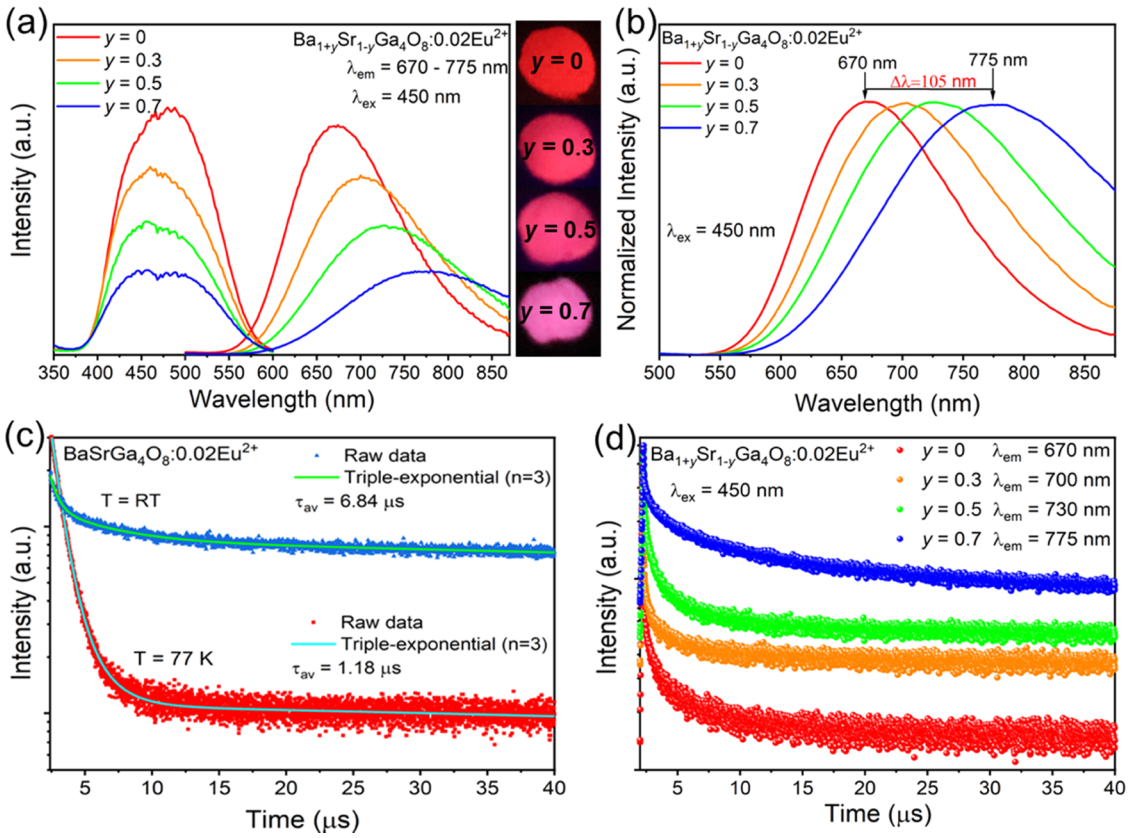

Figure 2. (a) Photoluminescence emission and excitation spectra of $Ba_{1+y}Sr_{1-y}Ga_4O_8:0.02Eu^{2+}$ (y = 0, 0.3, 0.5, 0.7) and photographs of the samples under 450 nm excitation. (b) Normalized emission spectra of $Ba_{1+y}Sr_{1-y}Ga_4O_8:0.02Eu^{2+}$($y$ = 0, 0.3, 0.5, 0.7) under 450 nm excitation. (c) Luminescence decay curves of $BaSrGa_4O_8:0.02Eu^{2+}$ upon excitation at 450 nm and monitored at 670 nm, measured at RT and 77 K, respectively. (d) Luminescence decay curves of of $Ba_{1+y}Sr_{1-y}Ga_4O_8:0.02Eu^{2+}$($y$ = 0, 0.3, 0.5, 0.7) measured at RT.

converged to 10^{-6} eV and 0.01 eV $Å^{-1}$, respectively. A 2 × 2 × 2 k-point grid was employed to sample the Brillouin zone, and the cutoff energy of the plane wave was set to 430 eV.

RESULTS AND DISCUSSION

$BaSrGa_4O_8$ crystallizes in hexagonal symmetry with the space group $P6_3$ (No. 173). The crystal structure consists of six-membered rings of GaO_4 tetrahedra on the ab plane, and the Ba/Sr atoms are located at the centers of the rings, as given in Figure 1a,b. Figure 1c displays the XRD patterns of the as-prepared $Ba_{1+y}Sr_{1-y}Ga_4O_8:0.02Eu^{2+}$ (y = 0, 0.3, 0.5, 0.7) measured at RT, which are highly consistent with the standard pattern (ICSD-95170),[26] with no detectable traces of impurity phases. The main diffraction peak shifts to a lower scattering angle with the gradual replacement of Ba for Sr, which can be attributed to lattice expansion caused by the substitution of the larger Ba^{2+}(IR = 1.47 Å, CN = 9) for the smaller Sr^{2+}(IR = 1.31 Å, CN = 9) in the same fold of coordination. Rietveld refinements of the XRD patterns were further conducted using the crystallographic data of $BaSrGa_4O_8$ as the starting model. The results are depicted in Figure 1d for the y = 0 sample and in Figure S1 for the other samples and are also listed in Table S2. The refinements showed good convergence with R_{wp} = 5.81% and R_p = 4.85% for $BaSrGa_4O_8$. The refined cell parameters increase linearly with increasing y, verifying the formation of solid solutions in accordance with Vegard's rule (Figure 1e). The fractional atomic coordinates, isotropic displacement parameters, and the main bond lengths for all of the samples are given in Tables S3 and S4. Figure 1f depicts the SEM image and EDS patterns of the selected $BaSrGa_4O_8:0.02Eu^{2+}$ sample. The smooth surface of the crystallite with a particle size of approximately 40 μm demonstrates its high crystallinity. Furthermore, the elemental mapping images show that Ba, Sr, Ga, O, and Eu are uniformly distributed in the $BaSrGa_4O_8:0.02Eu^{2+}$ phosphor particles. Finally, Figure S2 depicts the XRD patterns of $BaSrGa_4O_8:xEu^{2+}$ (x = 0.01−0.04) in comparison with the standard pattern, showing the high phase purity of the samples in the dopant concentration range.

The PL emission and excitation spectra of $BaSrGa_4O_8:xEu^{2+}$ (x = 0.01−0.04) at RT are displayed in Figure S3. Under blue light at 450 nm excitation, the emission spectra exhibit similar profiles extending from 550 to 870 nm with a maximum at 670 nm and FWHM = 140 nm. Normally, such broad emissions are related to the fact that Eu^{2+} ions are distributed at multiple sites, which will also be discussed later. Nevertheless, one can find from Figure S3 that the spectral profile remains invariable, indicating that the site distribution remains unchanged with varying Eu^{2+} contents. The corresponding excitation spectra show similar behaviors when monitoring the peak emission at 670 nm. The maximal emission or excitation intensity was found at x = 0.02, and a further increase in the doping concentration resulted in a decrease in the intensity due to concentration quenching. Therefore, the samples with 2% Eu^{2+} were chosen for further investigation. Moreover, the diffuse reflectance spectra and the fitting band gap were demonstrated in Figure S4, and the band gap value of $BaSrGa_4O_8$ by experimental fitting is determined to be 3.80 eV, and the Eu^{2+}

https://doi.org/10.1021/acs.chemmater.2c03631
Chem. Mater. 2023, 35, 1432−1439

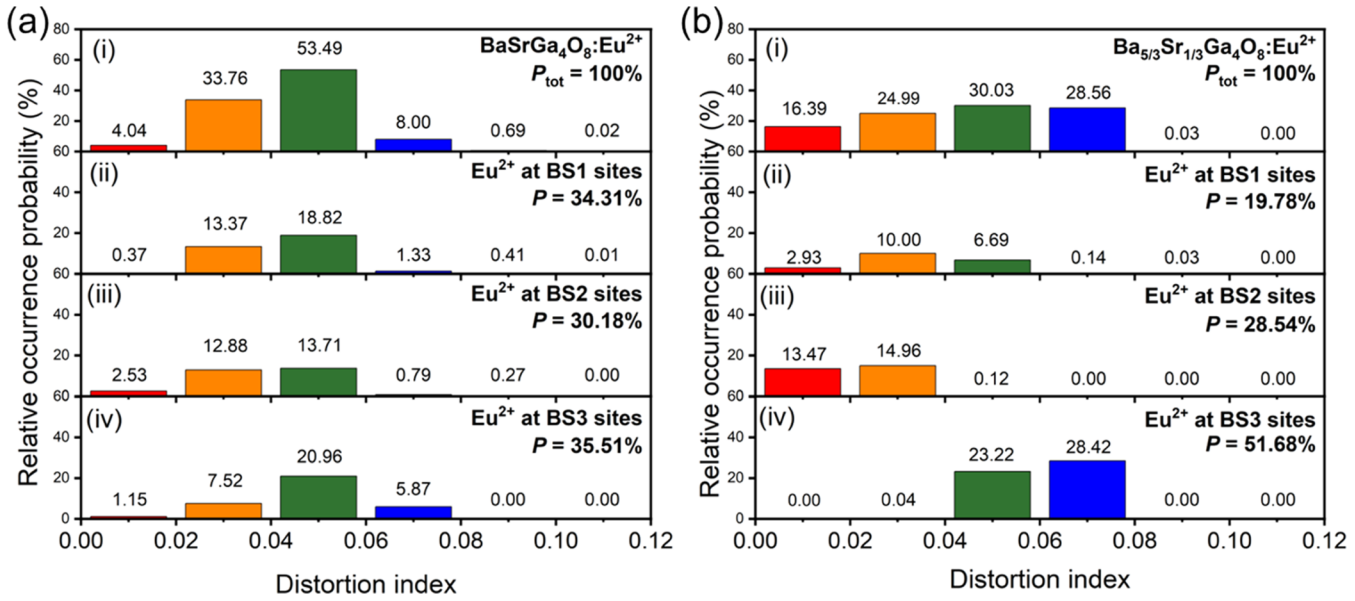

Figure 3. Calculated relative occurrence probabilities (P) against the distortion indices of the coordination polyhedra of Eu^{2+} at all BS sites (i) and at the BS1 (ii), BS2 (iii), and BS3 (iv) sites for $BaSrGa_4O_8$ (a) and $Ba_{5/3}Sr_{1/3}Ga_4O_8$ (b).

doping has little effect on this. Figure 2a depicts the variation of the emission and excitation spectra of $Ba_{1+y}Sr_{1-y}Ga_4O_8$:0.02Eu^{2+} at room temperature. With increasing y from 0.0 to 0.7, the emission band maximum exhibits a gradual red-shift from 670 to 775 nm, together with a band broadening from FWHM = 140 to 230 nm (Figure 2b). The spectral variation results in a gradual fading of the red emission color (side inset of Figure 2a). It is noted that the emission intensities decrease with increasing Ba content, and the intensity at y = 0.7 is only 35% of that at y = 0 (Figure S5). Moreover, the internal quantum efficiency (IQE) is also reduced from 28.6% at y = 0 to 20.8% at y = 0.7 (Table S6). This phenomenon is possibly related to a decrease of Eu^{2+} emission centers in the phosphors with increasing Ba content. Low-temperature (at 77 K) emission spectra were also measured for $Ba_{1+y}Sr_{1-y}Ga_4O_8$:0.02Eu^{2+} (y = 0 and 0.7), exhibiting a similar variation behavior with y as the room-temperature spectra (Figure S6). Furthermore, the luminescence decay behaviors of $BaSrGa_4O_8$:0.02Eu^{2+} monitored at peak wavelength 670 nm were measured at 77 K and RT (Figure 2c). The decay curves can be approximately fitted with triple-exponential functions,[27] and the derived average decay times are 1.12 μs (77 K) and 6.84 μs (RT), respectively, and the fitting parameters are given in Table S5. The low-temperature lifetime value agrees well with those observed for the normal Eu^{2+} 5d → 4f emission (around ∼1.0 μs),[28] and the much larger value at RT is probably related to thermally activated electron detrapping processes, which contributes to the lengthening of luminescence decay.[29] Figure 2d compares the luminescence decay behaviors of $Ba_{1+y}Sr_{1-y}Ga_4O_8$:0.02Eu^{2+} with y = 0, 0.3, 0.5, and 0.7 at room temperature. All of the curves can be fitted with triple-exponential functions and the average lifetime increases from 6.84 μs for y = 0 to 10.48 μs for y = 0.7 (Table S7).

To understand the connection between the Eu^{2+} emission properties and the nature of the local structure, DFT computations were first carried out for the Eu^{2+} site occupation and local coordination environments in $Ba_{1+y}Sr_{1-y}Ga_4O_8$ (y = 0 and 2/3). The occupation disorders on the three BS sites as well as the half occupancies of the two oxygen sites need to be modeled first. This was achieved by enumerating all possible configurations of Ba and Sr atoms in combination with the configurations of O atoms on the two half-occupied sites within the $Ba_{1+y}Sr_{1-y}Ga_4O_8$ unit cell. In $Ba_{1+y}Sr_{1-y}Ga_4O_8$, the atomic ratios Ba/Sr are 1 and 5 for y = 0 and 2/3, respectively, for which there are, in principle, 1280 and 384 configurations that reduce to 140 and 42 configurations after considering crystal symmetry.[30] For each crystallographically distinct configuration, an Eu atom was substituted at each of the six Ba or Sr sites, which totally generates 840 and 252 Eu-doped configurations for y = 0 and 2/3, respectively. The relative occurrence probabilities of these configurations were evaluated by $P_i = \frac{1}{Z}\Omega_i \exp\left(-\frac{E_i}{kT}\right)$, where E_i is the calculated DFT total energy, k is the Boltzmann constant, T = 1573 K is the material synthesis temperature, Ω_i is the configuration multiplicity, and Z is the partition function. Moreover, to elucidate the structure−property relationship, optimized structural properties around Eu^{2+} within a cutoff Eu−O bond length of 3.1 Å were also collected for each distinct configuration, such as the coordination number (CN), the average bond length (d_{av}), and the distortion index (DI), which are considered to represent the size and asymmetry of the site, respectively, when the CN remains invariant.[31]

For $BaSrGa_4O_8$:Eu^{2+}, out of the 840 configurations, 756 configurations have Eu^{2+} coordinated by six oxygens with a total occurrence probability (P) of 99.48%. The average Eu−O bond lengths are distributed in narrow ranges, with P = 92.84% for d_{av} = 2.50−2.60 Å and P = 5.04% for d_{av} = 2.60−2.70 Å. Similarly, among the 252 configurations for $Ba_{5/3}Sr_{1/3}Ga_4O_8$:Eu^{2+}, there are 227 configurations with Eu^{2+} coordinated by six oxygens, with a total P = 98.88%. The distribution of the average Eu−O bond lengths also lie in concentrated ranges, i.e., d_{av} = 2.50−2.60 Å (P = 86.58%) and 2.60−2.70 Å (P = 13.31%). These results indicate that the dopants Eu^{2+} in $Ba_{1+y}Sr_{1-y}Ga_4O_8$ are predominantly surrounded by six oxygens, despite the fact that the substitutional sites BS1−3 are nominally coordinated by nine oxygens in the

https://doi.org/10.1021/acs.chemmater.2c03631
Chem. Mater. 2023, 35, 1432−1439

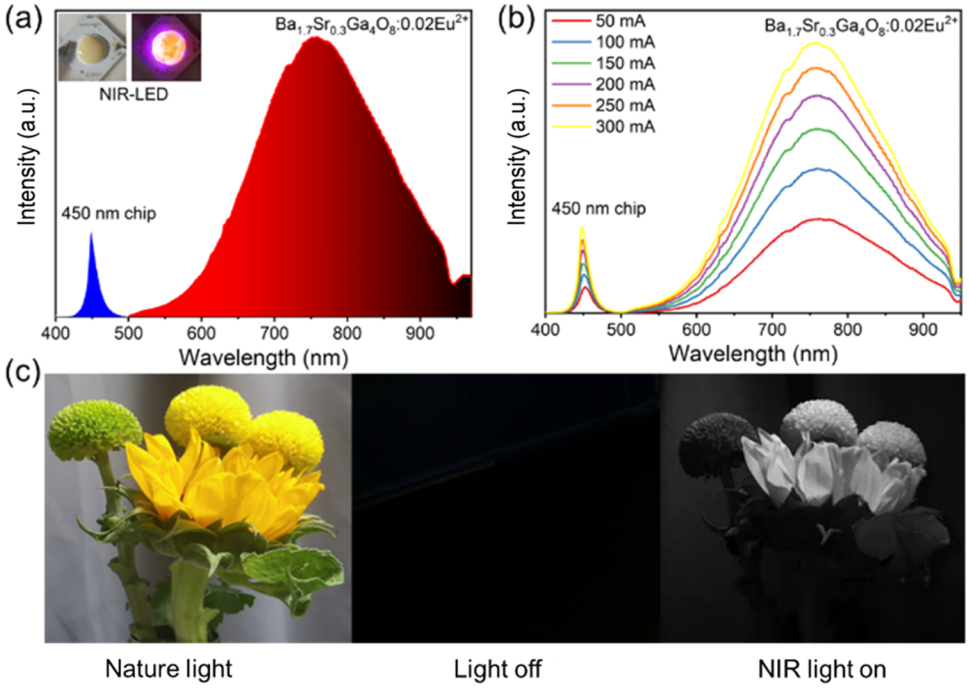

Figure 4. (a) Luminescence spectra and photographs of as-fabricated pc-LED fabricated by combining a commercial blue LED and the NIR-emitting $Ba_{1.7}Sr_{0.3}Ga_4O_8$:0.02Eu^{2+} phosphor. (b) Luminescence spectra of the fabricated pc-LED upon various forward bias currents. (c) Photographs taken under natural and NIR pc-LED light irradiations as captured by the visible and NIR cameras, respectively.

host crystal. It should be noted that the six-coordination of Eu^{2+} by oxygens is unusual, and in this case, the crystal-field splitting of the Eu^{2+} 5d level is larger than the common cases of higher seven- or eight-coordinations, which would lead to longer-wavelength 4f−5d absorption and emission even in the near-infrared spectral region,[28] as indeed experimentally observed in this work.

Next, we examined the observed emission maximum red shift and band broadening with increasing y for $Ba_{1+y}Sr_{1-y}Ga_4O_8$:Eu^{2+}. The $4f^65d^1$−$4f^7$ (5d−4f) emission (em) energy of Eu^{2+} can be expressed as $E_{em} = E_{ab} - \Delta S$, where E_{ab} denotes the lowest 4f−5d absorption (ab) transition energy and ΔS is the Stokes shift. E_{ab} is related to the centroid energy shift (ε_c) of the 5d configuration relative to the free ion and the 5d crystal-field splitting (ε_{cfs}), which are determined by the Eu−O covalency and the size of the coordination polyhedron, respectively. From the aforementioned computational results, the coordination numbers and the average Eu−O bond length are largely unchanged from $y = 0$ to 2/3 for $Ba_{1+y}Sr_{1-y}Ga_4O_8$:Eu^{2+}, which means that ε_c and ε_{cfs} and therefore E_{ab} would not change appreciably with increasing y. This result is in good agreement with the experimental observation that the excitation spectral profile is almost invariant for different $Ba_{1+y}Sr_{1-y}Ga_4O_8$:0.02Eu^{2+} (Figure S7).

On the other hand, a correlation has been made in the literature between the Stokes shift ΔS and the structural asymmetry of the dopant site.[32] It has been proposed that the coordination polyhedron of Eu^{2+} at an asymmetric site would rearrange significantly in the 5d excited state leading to a large ΔS. In this work, the site asymmetry is measured using the distortion index (DI) defined in terms of bond lengths, i.e.

$$\mathrm{DI} = \frac{1}{n}\sum_{i=1}^{n}\frac{|d_i - d_{av}|}{d_{av}}$$

where d_i is the ith Eu−O bond length and n is the CN.[33] Figure 3 depicts the relative occurrence probabilities against the distortion indices of Eu^{2+} coordination polyhedra in the enumerated configurations. It shows that for $BaSrGa_4O_8$:Eu^{2+}, the DIs are concentrated in the ranges of 0.02−0.04 (P = 33.76%) and 0.04−0.06 (P = 53.49%) (Figure 3a(i)), whereas for $Ba_{5/3}Sr_{1/3}Ga_4O_8$:Eu^{2+}, the DIs are evenly distributed over the range 0.00−0.08 (Figure 3b(i)). Especially, the total P for the configurations with large DI = 0.06−0.08 increases from 8.00% for $BaSrGa_4O_8$:Eu^{2+} to 28.56% for $Ba_{5/3}Sr_{1/3}Ga_4O_8$:Eu^{2+}. This indicates that there are more highly asymmetric Eu^{2+} sites in the latter compound with ensuing large Stokes shifts than in the former compound. Since a larger Stokes shift corresponds to a longer-wavelength and broader-band emission, the above finding suggests that the relative intensity of the long-wavelength portion of the emission spectrum for $Ba_{5/3}Sr_{1/3}Ga_4O_8$:Eu^{2+} is higher than that of $BaSrGa_4O_8$:Eu^{2+}, leading to a picture that the emission spectrum of $Ba_{5/3}Sr_{1/3}Ga_4O_8$:Eu^{2+} is redshifted and broadened with respect to that of $BaSrGa_4O_8$:Eu^{2+}. Thus, the gradual red shift and broadening of the emission spectrum of $Ba_{1+y}Sr_{1-y}Ga_4O_8$:Eu^{2+} with increasing y is due to the increase of the number of highly asymmetric Eu^{2+} sites, which results in a larger Stokes shift and thereby longer-wavelength and broader-band emission.

It is interesting to see if the above change in the P vs. DI distribution from $BaSrGa_4O_8$:Eu^{2+} to $Ba_{5/3}Sr_{1/3}Ga_4O_8$:Eu^{2+} is correlated with Eu^{2+} site occupations at the three BS sites. To investigate this further, the Eu^{2+} distribution was decomposed into the three sites. Figure 3a(ii−iv) shows that, in $BaSrGa_4O_8$, Eu^{2+} occupations at the BS1−3 sites have comparable occurrence probabilities, i.e., P = 34.31, 30.18, and 35.51%, respectively, and the P vs. DI distributions in the three cases are similar to each other and also to the overall distribution in Figure 3a(i). In contrast, in $Ba_{5/3}Sr_{1/3}Ga_4O_8$, the dopants Eu^{2+}

https://doi.org/10.1021/acs.chemmater.2c03631
Chem. Mater. 2023, 35, 1432−1439

are mainly located at BS3 sites with P = 51.68% (Figure 3b(iv)), and notably, the associated distortion indices are much larger than those for Eu^{2+} at BS1 and BS2 sites (Figure 3b(ii,iii)). One thus concludes that increasing the Ba/Sr atomic ratio from $BaSrGa_4O_8$ to $Ba_{5/3}Sr_{1/3}Ga_4O_8$ leads to a significant enhancement of Eu^{2+} occupancy at the BS3 site, which is characterized by relatively large DIs and ΔS, contributing dominantly to the red shift and broadening of the emission spectrum.

Finally, we recall and discuss the reason behind the increased tendency of Eu^{2+} occupation at the BS3 site with increasing y in $Ba_{1+y}Sr_{1-y}Ga_4O_8$:Eu^{2+}. Since the dopant Eu^{2+} is supposed to be substituted at the Sr^{2+} site rather than at the Ba^{2+} site due to size match, we calculated the Sr^{2+} distribution over the BS1−3 sites in the undoped compounds. It is found that the Sr occupancy ratios on the three BS sites are 0.93:0.93:1.14 for $BaSrGa_4O_8$ and 0.21:0.17:0.62 for $Ba_{5/3}Sr_{1/3}Ga_4O_8$, respectively. This indicates that the Ba excess induces a redistribution of Sr atoms on the three BS sites, with the BS3 site being preferred. This could be due to the relatively small size of the BS3 site (Figure 1b), which is favorable for Sr^{2+} rather than Ba^{2+} occupation. Therefore, the Sr^{2+} distribution on the BS1−3 sites regulates the Eu^{2+} distribution and thus the luminescence properties.

To further evaluate the thermal stability of the $Ba_{1+y}Sr_{1-y}Ga_4O_8$:0.02Eu^{2+} (y = 0, 0.7) phosphors, the temperature-dependent emission spectra in the temperature range of 25−200 °C were collected under 450 nm excitation (Figure S8a,b). The emission peak position presents a slight blue-shift because of the decrease in crystal-field strength, which is caused by gradual lattice expansion with increasing temperature. Moreover, the increased FWHM is related to the intensive electron−phonon interactions with increasing temperature. It can be clearly seen that the thermal stability of $Ba_{1.7}Sr_{0.3}Ga_4O_8$:0.02Eu^{2+} is slightly better than that of $BaSrGa_4O_8$:0.02Eu^{2+} (Figure S8c). A possible reason for this is that the introduction of Ba ions reduces the disorder of $BaSrGa_4O_8$, making its crystal structure more stable and hence improving its thermal stability.

A NIR pc-LED lamp was fabricated to illustrate the potential application by combining the $Ba_{1.7}Sr_{0.3}Ga_4O_8$:0.02Eu^{2+} phosphor and a commercial blue light-emitting InGaN chip. The broadband PL spectrum and the as-obtained and lit NIR pc-LED lamps at a forward bias current of 300 mA are given in Figure 4a. Figure 4b demonstrates the PL spectra of the LED device upon different forward bias currents (50−300 mA). The power efficiencies of the NIR LEDs have been measured depending on the current (Table S8), and one can find that the output power increases and reaches 14.6 mW@300 mA. Figure 4c displays photographs captured by visible and near-infrared cameras under natural and NIR pc-LED light irradiations. The color image of the flowers can be clearly detected under natural light irradiation but cannot be observed under dark conditions. By contrast, when the NIR pc-LED irradiation was adopted, the near-infrared camera can clearly capture black-and-white images of flowers. These results indicate that the achieved tunable $Ba_{1.7}Sr_{0.3}Ga_4O_8$:0.02Eu^{2+} phosphor has the application potential in night-vision technology.

CONCLUSIONS

In summary, Eu^{2+}-activated $Ba_{1+y}Sr_{1-y}Ga_4O_8$ (y = 0, 0.3, 0.5, 0.7) phosphors were successfully synthesized by a high-temperature solid-state reaction. Under the blue-light excitation at 450 nm, the phosphors exhibited an emission red-shift from 670 to 775 nm when the Ba contents were increased from y = 0 to 0.7, along with an increase of FWHM from 140 to 230 nm. The property regulation was elucidated on the basis of DFT calculations and attributed to more Eu^{2+} occupation on relatively highly asymmetric cationic sites, which is attributed to a combined structural effect of (i) Eu^{2+} substitution at small sites coordinated by six oxygens, (ii) greater diversity of Eu^{2+} local environments with increasing y, and (iii) larger Eu^{2+} local structural distortion caused by Ba excess. The concept of utilizing the host structure disorder to realize Eu^{2+} broadband emission is expected to open promising opportunities for developing NIR-emitting phosphors for multiple spectroscopy applications.

ASSOCIATED CONTENT

Supporting Information

The Supporting Information is available free of charge at https://pubs.acs.org/doi/10.1021/acs.chemmater.2c03631.

PXRD patterns; PL spectra; X-ray refinement; PLE spectra; temperature-dependent emission spectra; and other experimental data (PDF)

AUTHOR INFORMATION

Corresponding Authors

Lixin Ning − *Anhui Key Laboratory of Optoelectric Materials Science and Technology, Key Laboratory of Functional Molecular Solids, Ministry of Education, Anhui Normal University, Wuhu, Anhui 241000, China;* orcid.org/0000-0003-2311-568X; Email: ninglx@mail.ahnu.edu.cn

Zhiguo Xia − *The State Key Laboratory of Luminescent Materials and Devices, Guangdong Provincial Key Laboratory of Fiber Laser Materials and Applied Techniques, Guangdong Engineering Technology Research and Development Center of Special Optical Fiber Materials and Devices, School of Materials Science and Engineering and Department of Physics, South China University of Technology, Guangzhou 510641, China;* orcid.org/0000-0002-9670-3223; Email: xiazg@scut.edu.cn

Authors

Yingze Zhu − *The State Key Laboratory of Luminescent Materials and Devices, Guangdong Provincial Key Laboratory of Fiber Laser Materials and Applied Techniques, Guangdong Engineering Technology Research and Development Center of Special Optical Fiber Materials and Devices, School of Materials Science and Engineering, South China University of Technology, Guangzhou 510641, China*

Xuesong Wang − *Anhui Key Laboratory of Optoelectric Materials Science and Technology, Key Laboratory of Functional Molecular Solids, Ministry of Education, Anhui Normal University, Wuhu, Anhui 241000, China*

Jianwei Qiao − *The State Key Laboratory of Luminescent Materials and Devices, Guangdong Provincial Key Laboratory of Fiber Laser Materials and Applied Techniques, Guangdong Engineering Technology Research and Development Center of Special Optical Fiber Materials and Devices, School of Materials Science and Engineering, South China University of Technology, Guangzhou 510641, China*

Maxim S. Molokeev − *Laboratory of Crystal Physics, Kirensky Institute of Physics, Federal Research Center KSC SB RAS, Krasnoyarsk 660036, Russia; Institute of Engineering Physics*

and Radioelectronics, Siberian Federal University, Krasnoyarsk 660041, Russia; Department of Physics, Far Eastern State Transport University, Khabarovsk 680021, Russia; orcid.org/0000-0002-8297-0945

Hendrik C. Swart − *Department of Physics, University of the Free State, Bloemfontein ZA-9300, South Africa;* orcid.org/0000-0001-5233-0130

Complete contact information is available at: https://pubs.acs.org/10.1021/acs.chemmater.2c03631

Notes

The authors declare no competing financial interest.

■ ACKNOWLEDGMENTS

This research was supported by the National Key Research and Development Program of China (2021YFB3500400 and 2021YFE0105700), the National Natural Science Foundations of China (Grant Nos. 51972118, 11974022, and 52102169), the Local Innovative and Research Teams Project of Guangdong Pearl River Talents Program (2017BT01X137), the China Postdoctoral Science Foundation (2021M691053), and the Young Elite Scientists Sponsorship Program by China Association for Science and Technology (No. YESS20200053).

■ REFERENCES

(1) Guelpa, A.; Marini, F.; du Plessis, A.; Slabbert, R.; Manley, M. Verification of Authenticity and Fraud Detection in South African Honey Using NIR Spectroscopy. *Food Control* **2017**, *73*, 1388−1396.

(2) Fang, M.-H.; Li, T.; Huang, W.; Cheng, C.; Bao, Z.; Majewska, N.; Mahlik, S.; Yang, C.; Lu, K.; Leniec, G.; Kaczmarek, S. M.; Sheu, H.; Liu, R.-S. Surface-Protected High-Efficiency Nanophosphors via Space-Limited Ship-in-a-Bottle Synthesis for Broadband Near-Infrared Mini-Light-Emitting Diodes. *ACS Energy Lett.* **2021**, *6*, 659−664.

(3) De Beer, T.; Burggraeve, A.; Fonteyne, M.; Saerens, L.; Remon, J. P.; Vervaet, C. Near Infrared and Raman Spectroscopy for The In-Process Monitoring of Pharmaceutical Production Processes. *Int. J. Pharm.* **2011**, *417*, 32−47.

(4) Liu, G.; Xia, Z. Modulation of Thermally Stable Photoluminescence in Cr^{3+}-Based Near-Infrared Phosphors. *J. Phys. Chem. Lett.* **2022**, *13*, 5001−5008.

(5) Kim, D.; Jung, Y.; Toh, K. A.; Son, B.; Kim, J. An Empirical Study on Iris Recognition in a Mobile Phone. *Expert Syst. Appl.* **2016**, *54*, 328−339.

(6) De Guzman, G. N. A.; Fang, M.-H.; Liang, C.-H.; Bao, Z.; Hu, S.-F.; Liu, R.-S. [INVITED] Near-Infrared Phosphors and Their Full Potential: A Review on Practical Applications and Future Perspectives. *J. Lumin.* **2020**, *219*, No. 116944.

(7) Su, B.; Geng, S.; Xiao, Z.; Xia, Z. Highly Distorted Antimony(III) Chloride $[Sb_2Cl_8]^{2-}$ Dimers for Near-Infrared Luminescence up to 1070 nm. *Angew. Chem., Int. Ed.* **2022**, *61*, No. e202208881.

(8) Liu, G.; Hu, T.; Molokeev, M. S.; Xia, Z. Li/Na substitution and Yb^{3+} co-doping enabling tunable near-infrared emission in $LiIn_2SbO_6:Cr^{3+}$ phosphors for light-emitting diodes. *iScience* **2021**, *24*, No. 102250.

(9) Liu, G.; Molokeev, M. S.; Xia, Z. Structural Rigidity Control toward Cr^{3+}-Based Broadband Near-Infrared Luminescence with Enhanced Thermal Stability. *Chem. Mater.* **2022**, *34*, 1376−1384.

(10) Zhang, L.; Zhang, S.; Hao, Z.; Zhang, X.; Pan, G.-h.; Luo, Y.; Wu, H.; Zhang, J. A High Efficiency Broad-Band Near-Infrared $Ca_2LuZr_2Al_3O_{12}:Cr^{3+}$ Garnet Phosphor for Blue LED Chips. *J. Mater. Chem. C* **2018**, *6*, 4967−4976.

(11) Du, J.; Korthout, K.; Poelman, D.; De Clercq, O. Q. $LaAlO_3:Mn^{4+}$ as Near-Infrared Emitting Persistent Luminescence Phosphor for Medical Imaging: A Charge Compensation Study. *Materials* **2017**, *10*, No. 1422.

(12) Feng, G.; Zhou, S.; Bao, J.; Wang, X.; Xu, S.; Qiu, J. Transparent Ni^{2+}-Doped Lithium Aluminosilicate Glass−Ceramics with Broadband Infrared Luminescence. *J. Alloys Compd.* **2008**, *457*, 506−509.

(13) Wang, J. Environmentally Friendly Fe^{3+}-Activated Near-Infrared-Emitting Phosphors for Spectroscopic Analysis. *Light: Sci. Appl.* **2022**, *11*, No. 178.

(14) Sato, Y.; Kato, H.; Kobayashi, M.; Masaki, T.; Yoon, D. H.; Kakihana, M. Tailoring of Deep-Red Luminescence in $Ca_2SiO_4:Eu^{2+}$. *Angew. Chem., Int. Ed.* **2014**, *53*, 7756−7759.

(15) Zhao, M.; Yang, Z.; Ning, L.; Xia, Z. Tailoring of White Luminescence in a $NaLi_3SiO_4:Eu^{2+}$ Phosphor Containing Broad-Band Defect-Induced Charge-Transfer Emission. *Adv. Mater.* **2021**, *33*, No. 2101428.

(16) Zhao, M.; Zhang, Q.; Xia, Z. Structural Engineering of Eu^{2+}-Doped Silicates Phosphors for LED Applications. *Acc. Mater. Res.* **2020**, *1*, 137−145.

(17) Qiao, J.; Zhou, G.; Zhou, Y.; Zhang, Q.; Xia, Z. Divalent Europium-Doped Near-Infrared-Emitting Phosphor for Light-Emitting Diodes. *Nat. Commun.* **2019**, *10*, No. 5267.

(18) Li, S.; Amachraa, M.; Chen, C.; Wang, L.; Wang, Z.; Ong, S. P.; Xie, R.-J. Efficient near-infrared phosphors discovered by parametrizing the Eu(II) 5d-to-4f energy gap. *Matter* **2022**, *5*, 1924−1936.

(19) Bruker-AXS, T., v4: General Profile and Structure Analysis Software for Powder Diffraction Data. Karlsruhe, Germany 2008.

(20) Perdew, J. P.; Burke, K.; Ernzerhof, M. Generalized Gradient Approximation Made Simple. *Phys. Rev. Lett.* **1996**, *77*, 3865−3868.

(21) Canning, A.; Chaudhry, A.; Boutchko, R.; Gronbech-Jensen, N. First-Principles Study of Luminescence in Ce-Doped Inorganic Scintillators. *Phys. Rev. B.* **2011**, *83*, No. 125115.

(22) Dudarev, S. L.; Botton, G. A.; Savrasov, S. Y.; Humphreys, C. J.; Sutton, A. P. Electron-Energy-Loss Spectra and The Structural Stability of Nickel Oxide: An LSDA+U Study. *Phys. Rev. B* **1998**, *57*, 1505−1509.

(23) Kresse, G.; Furthmüller, J. Efficient Iterative Schemes Forab Initiottotal-Energy Calculations Using a Plane-Wave Basis Set. *Phys. Rev. B* **1996**, *54*, 11169−11186.

(24) Kresse, G.; Joubert, D. From Ultrasoft Pseudopotentials to The Projector Augmented-Wave Method. *Phys. Rev. B* **1999**, *59*, 1758−1775.

(25) Blöchl, P. E. Projector Augmented-Wave Method. *Phys. Rev. B* **1994**, *50*, 17953−17979.

(26) Kubota, S.; Takahashi, T.; Yamane, H.; Shimada, M. A powder X-ray Diffraction Study of A New Compound, $BaSrGa_4O_8$. *J. Alloys Compd.* **2002**, *345*, 105−109.

(27) Yang, Z.; Zhou, Y.; Qiao, J.; Molokeev, M. S.; Xia, Z. Rapid Synthesis of Red-Emitting $Sr_2Sc_{0.5}Ga_{1.5}O_5:Eu^{2+}$ Phosphors and The Tunable Photoluminescence via Sr/Ba Substitution. *Adv. Opt. Mater.* **2021**, *9*, No. 2100131.

(28) Qiao, J.; Ning, L.; Molokeev, M. S.; Chuang, Y. C.; Zhang, Q.; Poeppelmeier, K. R.; Xia, Z. Site-Selective Occupancy of Eu^{2+} toward Blue-Light-Excited Red Emission in a $Rb_3YSi_2O_7:Eu$ Phosphor. *Angew. Chem., Int. Ed.* **2019**, *58*, 11521−11526.

(29) Du, J.; Feng, A.; Poelman, D. Temperature Dependency of Trap-Controlled Persistent Luminescence. *Laser Photonics. Rev.* **2020**, *14*, No. 2000060.

(30) Grau-Crespo, R.; Hamad, S.; Catlow, C. R. A.; de Leeuw, N. H. Symmetry-Adapted Configurational Modelling of Fractional Site Occupancy in Solids. *J. Phys.: Condens. Matter* **2007**, *19*, No. 256201.

(31) Xia, Z.; Liu, Q. Progress in Discovery and Structural Design of Color Conversion Phosphors for LEDs. *Prog. Mater. Sci.* **2016**, *84*, 59−117.

(32) Wang, L.; Xie, R.; Suehiro, T.; Takeda, T.; Hirosaki, N. Down-Conversion Nitride Materials for Solid State Lighting: Recent Advances and Perspectives. *Chem. Rev.* **2018**, *118*, 1951−2009.

(33) Baur, W. H. The Geometry of Polyhedral Distortions. Predictive Relationships for The Phosphate Group. *Acta Crystallogr., Sect. B: Struct. Crystallogr. Cryst. Chem.* **1974**, *30*, 1195−1215.

https://doi.org/10.1021/acs.chemmater.2c03631
Chem. Mater. 2023, 35, 1432−1439